Research Square

Preprints are preliminary reports that have not undergone peer review.
They should not be considered conclusive, used to inform clinical practice,
or referenced by the media as validated information.

Na/Fe-Modified Natural Bentonite as a Photo-Fenton-like Catalyst for Abamectin Degradation in Water and Soil

maryam moosavifar

m.moosavifar90@gmail.com

University of Maragheh

masoumeh dibazar

University of Maragheh

Article

Keywords: Na/Fe-modified bentonite, abamectin, photo-Fenton-like process, hydrogen peroxide, reusable catalyst

Posted Date: November 24th, 2026

DOI: https://doi.org/10.21203/rs.3.rs-11680983/v1

License: This work is licensed under a Creative Commons Attribution 4.0 International License.
Read Full License

Additional Declarations: No competing interests reported.

Na/Fe-Modified Natural Bentonite as a Photo-Fenton-like Catalyst for Abamectin Degradation in Water and Soil

Maryam Moosavifar*[,1], Masoumeh Dibazar[1]

[1]Department of Chemistry, Faculty of Science, University of Maragheh, P.O. Box 55181-83111, Maragheh, Iran

Abstract

Abamectin is an environmental contaminant of serious concern. In this study, a naturally occurring bentonite from the Ardabil mine was modified with Fe(II) and evaluated as a heterogeneous photo-Fenton catalyst for abamectin degradation. Characterization (XRD, FTIR, BET, SEM, EDS) confirmed successful iron incorporation and a mesoporous structure with a specific surface area of 34.92 $m^2\ g^{-1}$.

Operating under UV/H_2O_2, the system overcame acidic limitations, achieving optimal efficiency at natural neutral pH (pH = 7.0) with 0.03 g catalyst, 100 mg L^{-1} abamectin, and 20 µL H_2O_2. Degradation followed pseudo-first-order kinetics ($k = 0.0089\ min^{-1}$, $R^2 = 0.964$ at 25 °C). COD removal reached 73.9%, achieving significant mineralization accompanied by improved biodegradability (BOD_5/COD 0.125 → 0.135). The catalyst remained highly stable over six consecutive cycles, with negligible iron leaching. Applicability was further examined with a commercial abamectin formulation and in soil pot experiments exposed to sunlight. These findings establish the low-cost Na/Fe-modified bentonite as a robust, recoverable catalyst for remediating persistent pesticide-contaminated environments.

Keywords: Na/Fe-modified bentonite; abamectin; photo-Fenton-like process; hydrogen peroxide; reusable catalyst.

1. Introduction

The expansion of intensive agricultural practices to ensure food security has significantly increased the discharge of pesticides into surface and groundwater resources [1-3]. Among these contaminants, abamectin, a macrocyclic insecticide/acaricide derived from the avermectin family, has emerged as a significant environmental concern. Due to its complex stereochemical structure

* Corresponding author: E-mail: m.moosavifar90@gmail.com, moosavifar@maragheh.ac.ir Tel: +98-421-2273068, fax: +98-421-2276060

($C_{48}H_{72}O_{14}$) and high molecular weight, abamectin exhibits substantial resistance to natural degradation and biodegradation [4]. It is known to possess high acute toxicity, even at microgram-per-liter concentrations, for non-target aquatic organisms such as *Daphnia magna* [5]. Given its persistent organic pollutant (POP) nature and potential for bioaccumulation, developing remediation technologies for abamectin-contaminated water and soil are an environmental imperative [6-10].

Conventional treatment methods, including biological processes, coagulation–flocculation, and activated carbon adsorption, often fail to completely mineralize such stable compounds, frequently resulting in phase transfer rather than molecular destruction. Consequently, Advanced Oxidation Processes (AOPs), driven by the generation of highly reactive hydroxyl radicals ($\cdot OH$, $E^0 = 2.80$ V), have gained prominence for the degradation of recalcitrant organic contaminants [5, 10]. Among AOPs, Fenton and photo-Fenton reactions are highly regarded for their efficiency in decomposing organophosphorus and macrocyclic compounds [11, 12].

However, traditional homogeneous Fenton processes face critical operational limitations: (1) the strict requirement for acidic pH to prevent iron hydroxide precipitation, (2) the generation of hazardous iron sludge as secondary waste, and (3) the inability to recover the catalyst [13, 14]. These drawbacks significantly hinder field-scale applications, particularly where treatment must occur at near-neutral pH, such as in agricultural drainage or soil remediation [13]. To address these challenges, heterogeneous Fenton-like systems have been developed by immobilizing transition metals onto solid supports, such as natural aluminosilicates, to create localized acidic micro-environments and facilitate catalyst recovery [9, 13, 16].

Bentonite, primarily composed of 2:1 layered montmorillonite, possesses unique physicochemical properties that make it a highly promising candidate for environmental remediation technologies. The permanent negative lattice charge, resulting from isomorphic substitutions (such as Al^{3+} for Si^{4+} and Mg^{2+} for Al^{3+}), is balanced by exchangeable cations such as Na^{+} or Ca^{2+} situated within the interlayer spaces [15]. This structural feature positions bentonite as a potential host for the immobilization of catalytically active species, where the interlayer galleries can function as micro-reactors to stabilize metal ions and prevent their agglomeration. Notably, sodium-rich bentonites, characterized by high swelling capacity and significant cation exchange capacity (CEC), offer enhanced accessibility for the incorporation of transition metal cations [17]. Theoretically, the

substitution of natural interlayer cations with active transition metals within this aluminosilicate framework could create catalytic sites capable of facilitating H_2O_2 decomposition and $^{\bullet}OH$ generation via surface redox cycles [18]. These attributes, combined with its natural abundance and cost-effectiveness, make bentonite a strategic platform for developing heterogeneous catalysts that aim to overcome the inherent limitations of conventional Fenton processes.

Despite the demonstrated potential of clay-based heterogeneous Fenton systems, the application of raw, unprocessed mining-grade bentonite as a direct precursor for catalyst synthesis — without extensive purification — remains underexplored [19]. Furthermore, the performance of such systems toward complex macrocyclic pesticides like abamectin, particularly across diverse environmental matrices including contaminated soils, has not been systematically assessed [20].

To address these research gaps, this study explains raw mining-grade sodium bentonite sourced from Ardabil mines as an abundant and cost-effective natural resource for developing a heterogeneous Fe(II)/Bentonitecatalyst. To improve operational efficiency, raw bentonite was rapidly prepared into its sodium-homoionic form, which effectively enhanced interlayer swelling and cation-exchange capacity and optimized the loading of active sites. The core novelty of this work lies in the application of this engineered platform within a photo-Fenton system for the effective degradation and partial mineralization of abamectin under unadjusted, near-neutral pH conditions. This approach successfully overcomes the inherent limitations of conventional Fenton processes, including the narrow acidic pH window and problematic sludge formation. Beyond rigorous kinetic modeling and real-time mineralization tracking via COD reduction and biodegradability assessment, the practical efficacy of the system was further examined with a commercial abamectin formulation and, notably, in soil pot experiments [21]. Finally, the structural stability and reusability of the catalyst over consecutive cycles were assessed, providing a comprehensive evaluation of its potential for the cost-effective remediation of contaminated aquatic and terrestrial ecosystems.

2. Experimental

2.1. Materials and reagents

A naturally occurring mixed Na/Ca-bentonite sourced directly from the Ardebil mine ([Ardebil], Iran), without prior industrial processing, was used as the parent clay. To ensure interlayer cation homogeneity and maximize basal spacing, the raw bentonite was subjected to 0.5M an aqueous sodium chloride solution, followed by washing with deionized water until free of Cl^- ions (confirmed by $AgNO_3$ test), and drying at 80 °C for 24 h. The resulting homoionized Na-bentonite was then used as the support for iron loading.

All chemicals, including hydrogen peroxide (H_2O_2, 30% w/w), sulfuric acid (H_2SO_4, 98%), hydrochloric acid (HCl, 37%), oxalic acid ($H_2C_2O_4$), potassium nitrate (KNO_3), and potassium permanganate ($KMnO_4$) purchased from Merck and Sigma-Aldrich. Sodium hydroxide (NaOH) and sodium chloride (NaCl) were of analytical grade and used as received without further purification. Abamectin (analytical grade, purity ≥ 98%) was used as the target contaminant, and stock solutions were prepared at concentrations of 50–250 mg L^{-1}. In addition to analytical-grade abamectin, we used a commercially formulated product (Vertimec® 1.8% EC, Syngenta; active ingredient: 18 g L^{-1} abamectin as an emulsifiable concentrate) to assess degradation performance under conditions representative of real agricultural runoff.

2.2. Characterization Techniques

The synthesized iron-modified bentonite was characterized using a comprehensive suite of complementary analytical techniques. Fourier-transform infrared spectroscopy (FT-IR; Thermo Nicolet iS10, USA) was employed to identify surface functional groups and monitor structural perturbations induced by iron loading, with spectra recorded in the wavenumber range of $400 - 4000\ \mathrm{cm}^{-1}$ using the KBr pellet method. Crystalline phase composition and basal d-spacing values were determined by X-ray powder diffraction (XRD; Bruker D8 Advance, Germany) using Cu Kα radiation ($\lambda = 0.15406$ nm) operated at 40 kV and 40 mA across the 2θ range of $3° - 80°$. Surface morphology and elemental distribution were examined by field-emission scanning electron microscopy coupled with energy-dispersive X-ray spectroscopy (FE-SEM/EDS; TESCAN MIRA3, Czech Republic). Specific surface area, total pore volume, and average pore diameter were determined from nitrogen (N_2) adsorption–desorption isotherms at 77 Kusing the Brunauer–Emmett–Teller (BET) method and the Barrett–Joyner–Halenda (BJH) model (Quantachrome Nova 2200e, USA), following degasification under vacuum. The concentration of

iron species leached into the aqueous medium during catalytic degradation was quantitatively tracked by inductively coupled plasma optical emission spectrometry (ICP-OES; Varian Vista-PRO, Australia).

2.3. Preparation of Na/Fe-bentonite catalyst

The Na/Fe-modified bentonite (Na/Fe-bentonite) catalyst was synthesized via a two-step ion-exchange procedure applied to the raw natural Na/Ca-bentonite. In the first step, approximately 2 g of raw bentonite powder was dispersed in 100 mL of 0.5 M NaCl solution in a 250 mL beaker and stirred magnetically at room temperature for 24 h. The resulting solid was filtered and washed repeatedly with hot distilled water until no residual chloride ions were detectable (confirmed by a 0.01 M $AgNO_3$ solution test). The Na-bentonite was then dried at 80 °C for 24 h and stored in a desiccator until use. In the second step, 2 g of the dried Na-bentonite was dispersed in 100 mL of 0.5 M $FeCl_2$ solution and stirred magnetically at room temperature for 24 h to promote Fe^{2+} exchange into the interlayer space. The solid was recovered by filtration, washed thoroughly with distilled water to remove residual chloride ions (confirmed by $AgNO_3$ test), and dried at 100 °C for 2 h. The resulting Na/Fe-bentonite was stored in a desiccator and used as the heterogeneous photo-Fenton catalyst for all subsequent degradation experiments.

2.4. Photocatalytic degradation and stability tests

Photocatalytic degradation experiments were carried out in a custom-built photoreactor equipped with a UV lamp (15 W, λ_{max} = 254 nm), a cylindrical glass reaction vessel, and a magnetic stirrer. In a typical reaction run, a specified amount of Na/Fe-bentonitecatalyst was dispersed in 100 mLof aqueous abamectin solution, followed by the addition of hydrogen peroxide. Before UV irradiation, the suspension was stirred continuously in the dark for 30 minto attain adsorption–desorption equilibrium between the contaminant and the catalyst surface. Upon initiating UV irradiation, aliquots were sampled at regular 30-minintervals over a total reaction time of 180 min. The solid catalyst was separated by centrifugation, and the residual abamectin concentration was monitored using UV–Vis spectrophotometry at its maximum absorption wavelength ($\lambda_{\max}$ = 257 nm) across the scanning range of 200–350 nm. To evaluate the parametric effects and optimize the photo-Fenton performance, operational parameters were systematically varied within

the following ranges: initial pollutant concentration (50–250 mg L^{-1}), catalyst dosage (0.01–0.04 g), H_2O_2 volume (15–23 µL) (1:17 ratio), and solution pH (4–9). To evaluate catalyst stability and confirm the heterogeneous nature of the reaction, a catalytic leaching test was conducted under representative conditions: after 30 minof reaction, the solid catalyst was completely removed from the suspension via filtration, and the reaction progress of the clear filtrate was monitored for an additional 150 min. Before ICP-OES analysis, liquid samples were passed through a 0.45 μm PTFE syringe filter and acidified with concentrated $HNO_3$to prevent iron precipitation.

2.5. Soil remediation studies

To evaluate the practical applicability of the developed Na/Fe-bentonite system in complex real-world matrices, the optimized photocatalytic procedure was extended to a formulated abamectin sample (100 mg L^{-1}). Furthermore, the catalytic performance in soil was assessed through a series of pot experiments. A comparative study was conducted utilizing four distinct treatments: untreated soil (control), soil amended with natural bentonite, soil amended with Na-bentonite, and soil amended with the optimized Na/Fe-bentonite. Soil samples were collected at predetermined intervals (1, 24, and 72 h, as well as 10 d) to monitor temporal pesticide degradation. The soil extracts were separated from the solid phase, and the residual abamectin concentration was determined via UV–Vis spectrophotometry, allowing for a quantitative comparison of degradation kinetics and efficiency across the different soil-amended treatments. The soil pots were kept outdoors under natural solar irradiation during the summer season (approximately August–September). Ambient temperature, relative humidity, and rainfall were not recorded during the exposure period; therefore, the soil results reflect uncontrolled field-like conditions and cannot be separated from weather variability.

2.6. Chemical Oxygen Demand (COD) and Biochemical Oxygen Demand (BOD_5) determination

COD was determined by the potassium permanganate titrimetric method [22]. Briefly, 100 mL of sample was acidified with 5 mL of concentrated sulfuric acid and heated at 100 °C for 5 min. A volume of 20 mL of 0.04 M $KMnO_4$was then added, and the mixture was boiled for a further 10

min. Following the addition of 20 mL of 0.04 M oxalic acid, back-titration was performed against standardised $KMnO_4$at approximately 80 °C. The COD value was calculated as:

$$\mathrm{COD} = \frac{(a-b) \times f \times 316}{V} \qquad \text{(Eq. 1)}$$

where $a$and b(mL) are the volumes of $KMnO_4$consumed for the sample and blank, respectively; $f$is the correction factor of the $KMnO_4$ solution; and V(mL) is the sample volume.

BOD_5 was determined by the iodometric (Winkler) method. Dilution water was prepared with nutrient stock solutions comprising phosphate buffer, $MgSO_4$, $CaCl_2$, and $FeCl_3$ [23]. Diluted samples were dispensed into dark-stoppered BOD bottles in duplicate; one set was fixed immediately for the initial dissolved oxygen (D_1) measurement by adding $MnCl_2$solution followed by alkaline NaN_3/KIreagent, while the remaining set was incubated in the dark at 20 ± 1 °C for 5 days. After incubation, the same fixation procedure was applied to yield the final dissolved oxygen (D_2). In both cases, the resulting precipitate was dissolved with phosphoric acid, and the liberated iodine was titrated with 0.01 M sodium thiosulfate using starch–zinc iodide as an indicator. The BOD_5value (mg L^{-1}) was determined using Eq. (2):

$$\mathrm{BOD_5\ (mg\ L^{-1})} = \left(\frac{V_a}{V_b}\right) \times \left(Z_p - Z_v\right) + Z_v \qquad \text{(Eq. 2)}$$

where V_a(mL) is the total volume after dilution, V_b(mL) is the initial sample volume, and $D_1$and D_2 (mg L^{-1}) are the dissolved oxygen concentrations at $t = 0$ and $t = 5$ days, respectively. $Z_p = D_1 - D_2$ is the DO depletion in the diluted sample, $Z_v = B_1 - B_2$ is the DO depletion in the blank dilution water, and $P = \frac{V_b}{V_a}$ is the dilution fraction.

3. Result and discussion

3.1. Characterization of Na/Fe-modified bentonite

The heterogeneous catalyst was synthesized via a sequential two-step cation-exchange route. As established in clay mineralogy [24], pristine smectites predominantly harbor divalent interlayer cations (mainly Ca^{2+}), whose high hydration energy and strong electrostatic interactions restrict

interlayer expansion and mass transport. Consequently, the pristine clay was initially subjected to Na-homoionization to exchange divalent species with monovalent Na^+ions, thereby enhancing structural delamination and basal spacing. In the subsequent stage, active iron species were incorporated into the expanded interlayer galleries and surface sites via ion exchange to establish catalytic centers for the heterogeneous Fenton-like degradation of abamectin.

The chemical composition of the raw bentonite, determined by XRF, is provided in **Table S1**. As expected, SiO_2 and Al_2O_3 constitute the major framework oxides, consistent with a typical 2:1 dioctahedral montmorillonite structure, while CaO (1.90 wt%) is dominant over Na_2O (0.59 wt%) corroborates the Ca-rich nature of the native bentonite. Following modification, the elemental composition of the Na/Fe-bentonite was probed via EDS microanalysis (Table **S2**), exhibiting a distinct Fe content of 13.91 wt% (7.64 at%), accompanied by 49.12 wt% Si and 21.78 wt% Al.

To rigorously evaluate the compositional evolution and eliminate analytical discrepancies arising from the differing sampling depths of bulk XRF versus near-surface EDS, characteristic structural mass ratios were followed (Table 1). The Si/Al ratio (2.26) confirms that the structural integrity of the layered aluminosilicate skeleton was preserved without framework collapse. Crucially, the notable increase of the Fe/Si ratio from 0.106 in raw bentonite to 0.283 in Na/Fe-bentonite clay strongly supports the successful incorporation and enrichment of active iron species across the aluminosilicate matrix. Moreover, the subtle vibrational shoulder observed near 880 cm^{-1} in the FT-IR spectrum can be tentatively attributed to structural Al-Fe-OH bending modes, consistent with the coordinated integration of iron centers within the clay structure. By maintaining mild synthesis conditions and omitting harsh thermal calcination, structural collapse was prevented, keeping active iron sites readily accessible for driving heterogeneous Fenton-like oxidation cycles.

Table 1. Key structural and compositional mass ratios of raw bentonite (derived from XRF) and synthesized Na/Fe-bentonite (derived from EDS)

Elemental Ratio[a]	Raw Bentonite (XRF)	Fe-Bentonite (EDS)	Scientific Interpretation
Si / Al	1.33	2.26	Characteristic stoichiometric 2:1 layer (for smectites Si/Al 2-4)
Fe / Si	0.106	0.283	↑ 2.7 ×(Fe loading)
Na / Ca	0.32	1.76	↑ 5.5 ×(Na-homoionization)
Fe / Ca	3.97	9.94	(Interlayer active exchange)

[a] Elemental weight fractions for pristine bentonite were calculated from the bulk oxide XRF data (Table S1), whereas Na/Fe-bentonite values were acquired via localized EDS microanalysis (Table S2).

In addition, considerable increase in the Na/Ca ratio from 0.32 to 1.76, along with the surge in the Fe/Ca ratio from 3.97 to 9.94, provides conclusive evidence of efficient interlayer Ca^{2+}displacement and effective transition-metal functionalization.

The X-ray diffraction patterns of the pristine bentonite and the synthesized Na/Fe-modified bentonite catalyst are shown in Fig. 1a and 1b, respectively. In the low-angle region, the Na/Fe-bentonite displays a well-defined basal reflection at $2\theta = 4.20°$, corresponding to an expanded interlayer basal spacing of $d_{001} = 21.02$ Å calculated via Bragg's law. Compared with the typical basal spacing of pristine natural bentonite (12.5-15 Å) [24, 25], this substantial interlayer expansion confirms the successful intercalation and stabilization of hydrated iron species and poly-hydroxy-iron oligomers within the smectite interlayer galleries.

Furthermore, the preservation of the asymmetric reflection at $2\theta = 60.60°$, which serves as the characteristic structural fingerprint of dioctahedral smectites, verifies that the parent 2:1 aluminosilicate layer framework was preserved without layer collapse during the modification steps [26].

In the wide-angle region ($2\theta = 10° - 80°$), the broad reflection centered near $2\theta \approx 21.90°$ corresponds to disordered opal-CT/cristobalite, while a secondary reflection at $2\theta = 26.40°$is indexed to residue crystalline quartz [27]. Crucially, no sharp diffraction peaks attributable to discrete crystalline iron oxides or oxyhydroxides (such as hematite or goethite) were observed, evidencing that the active iron centers exist as highly dispersed species rather than bulky agglomerates. This favorable dispersion is fully consistent with the omission of any calcination

step and the preservation of the native clay framework. From a catalytic standpoint, such structural characteristics are highly advantageous, as they maximize the accessibility of the active Fe^{2+}/Fe^{3+}sites required to sustain the heterogeneous Fenton-like degradation cycle [28].

The FT-IR spectrum of the Na/Fe-modified bentonite catalyst (Fig. 1c) shows characteristic vibrational signatures of a dioctahedral smectite in the 400−4000 cm^{-1} range. The broad, prominent absorption band centered at 3445 cm^{-1}, along with the bending vibration at 1631 cm^{-1}, corresponds to the H-O-H stretching and bending modes of interlayer and physisorbed water molecules. The subtle shoulder at 3620 cm^{-1} is assigned to the structural O-H stretching of octahedral Al_2OH groups, which is modulated by local coordination with Fe-OH species. The predominant lattice vibration at 1092 cm^{-1} is attributed to the asymmetric Si–O–Si stretching of

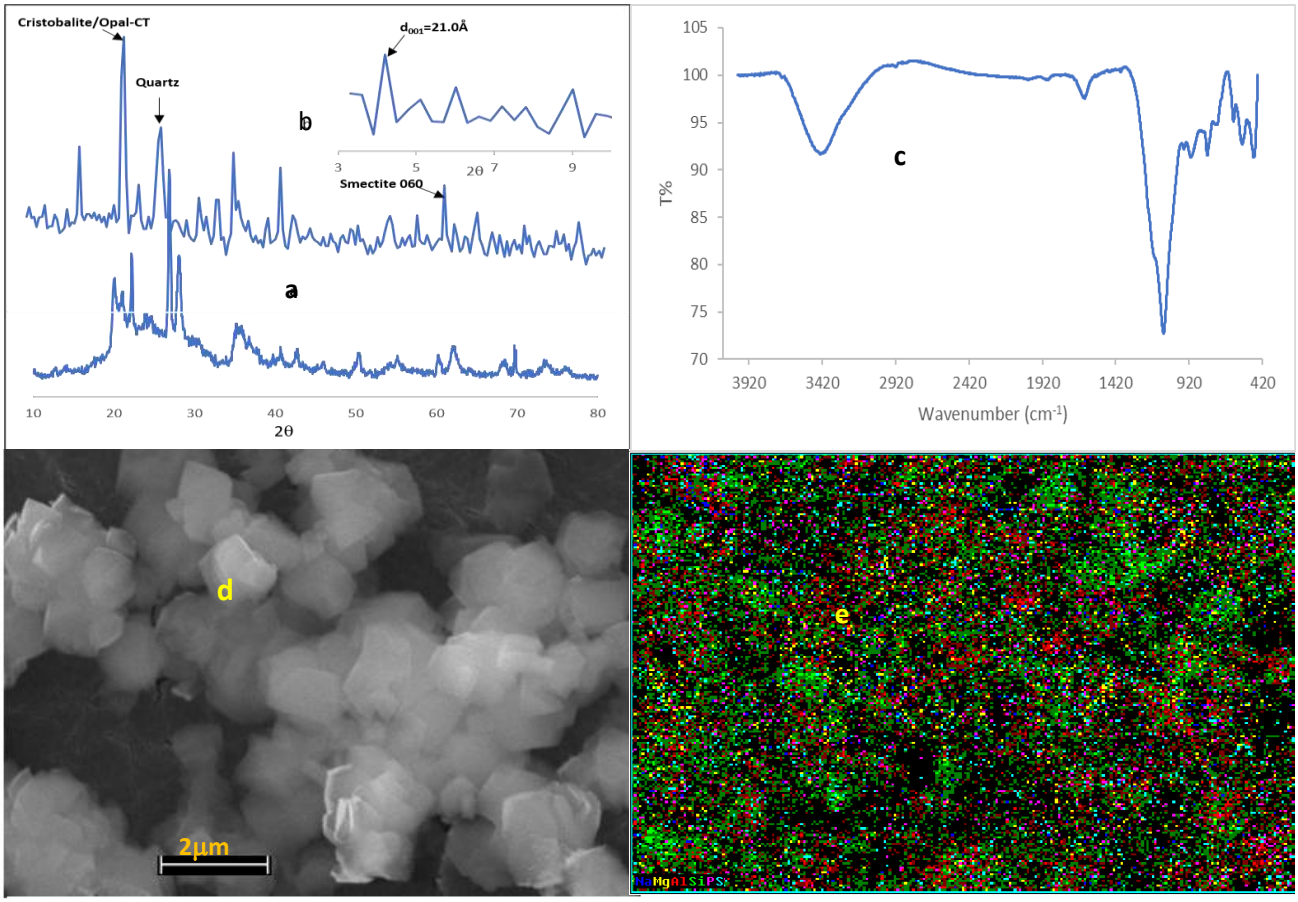

Fig. 1. Powder X-ray diffraction (XRD) patterns of (a) raw bentonite and (b) synthesized Na/Fe-modified bentonite catalyst, (c) FT-IR spectrum of the Na/Fe-modified bentonite catalyst, (d) FESEM micrograph, and (e) corresponding overlaid elemental distribution map of the Na/Fe-modified bentonite catalyst.

the tetrahedral framework [29]. The noticeable shift of this primary band from the conventional montmorillonite range (1030–1040 cm^{-1}) toward 1092 cm^{-1}, accompanied by a distinct shoulder near 1114 cm^{-1}, reflects local symmetry lowering of the SiO_4 tetrahedra induced by interlayer Fe^{3+} cations (splitting of the degenerate Si–O stretching modes into in-plane and out-of-plane components), along with convolution from asymmetric stretching vibrations of coexisting silica phases (opal-CT / free silica). We assign the band at 907 cm^{-1} to octahedral Al-Al-OH bending deformation, while the doublet at 794 and 779 cm^{-1} confirms the presence of crystalline quartz as an accessory mineral [30]. The low-frequency bands at 556 cm^{-1} (Al-O-Si bending) and 478 cm^{-1} (Si-O-Si bending) indicate that the layered phyllosilicate skeleton remains intact after modification [29]. Finally, the subtle feature near 880 cm^{-1} is tentatively assigned to AlFe-OH bending, validating the successful incorporation and immobilization of Fe^{3+} species onto the clay matrix [30].

The surface morphology and elemental distribution of the Na/Fe-modified bentonite catalyst are illustrated in Fig. 1dand 1e. The FESEM micrograph (Fig. 1d) reveals an aggregated, layered morphology characteristic of the phyllosilicate framework, featuring stacked plate-like sheets with irregular edges. The overlaid elemental map (Fig. 1e) demonstrates a uniform and well-dispersed distribution of the constituent framework elements alongside the immobilized iron species across the examined matrix, confirming successful and homogeneous incorporation of iron without noticeable phase segregation. The corresponding EDS spectrum and individual elemental distribution maps are provided in the Supplementary Information (**Figs. S1** and **S2**).

The surface textural characteristics and porosity of the synthesized Na/Fe-bentonite were determined via N_2 adsorption–desorption measurements at 77 K, as summarized in Table 2 and illustrated in Fig. 2.

As shown in Fig. 2a**,** the adsorption isotherm exhibits a typical Type IV profile according to the IUPAC classification, which is characteristic of mesoporous materials [29]. A distinct H3-type hysteresis loop is observed in the relative pressure range of P/P_0= 0.45-0.99. This hysteresis pattern is widely recognized in 2:1 smectite clays and is associated with capillary condensation within non-rigid aggregates of plate-like particles that give rise to slit-shaped mesoporous galleries [29]. The rapid and steep surge in nitrogen uptake near saturation pressure ($P/P_0 > 0.90$) reveals the

presence of large textural interparticle macropores, which is in excellent agreement with the aggregated flake-like morphology revealed by FESEM.

Table 2. Textural properties of Na/Fe-modified bentonite derived from N_2 physisorption analysis.

Parameter	BET Specific Surface Area (S_{BET})($m^2 g^{-1}$)	Mesopore Cumulative Volume (BJH adsorption) V_{meso} ($cm^3 g^{-1}$)	BET Constant (C)	Peak Pore Radius r_p (BJH peak) (nm)
Value	34.92	0.156	5.443	1.25

According to Table 2, the BET specific surface area (S_{BET}) and the cumulative mesopore volume (derived from the BJH adsorption branch) of the Na/Fe-bentonite catalyst were calculated to be 34.92 $m^2 g^{-1}$ and 0.156 $cm^3 g^{-1}$, respectively. The preservation of this considerable surface area confirms that the two-step ion-exchange functionalization with Fe^{3+} cations proceeded successfully without severe channel plugging or exfoliation collapse of the smectite interlayer galleries [19]. Furthermore, the BJH pore size distribution curve (Fig. 2b) demonstrates a narrow distribution with a primary peak radius at $r_p \approx 1.25$ nm (equivalent to a pore diameter of ca. 2.5 nm), confirming a well-developed mesoporous framework. This interconnected mesoporous

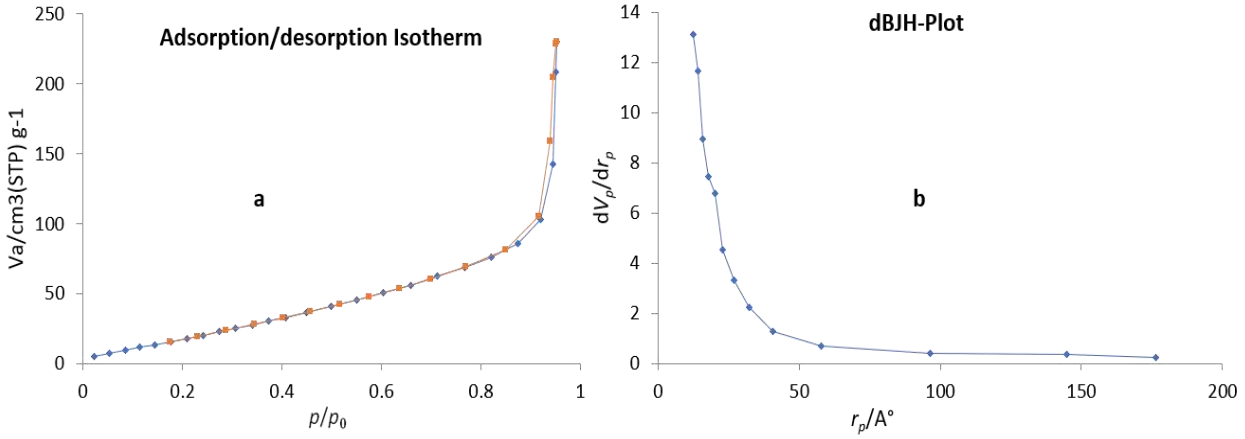

Fig. 2. (a) N_2 adsorption–desorption isotherm and (b) BJH pore size distribution of the Na/Fe-modified bentonite sample.

network is critical for the heterogeneous photo-Fenton process, as it facilitates rapid mass transfer of bulky abamectin molecules and H_2O_2 toward the accessible Fe^{3+}/Fe^{2+} redox centers. These

active sites are distributed across both the external particle surfaces and the interlayer basal planes of the smectite structure.

3.2. Photocatalytic and photo-Fenton degradation of abamectin

The photocatalytic performance of Na/Fe-modified bentonite was evaluated through the degradation of abamectin under UV irradiation in the presence of hydrogen peroxide. To maximize degradation efficiency and elucidate the underlying reaction mechanism, we systematically optimized key operational parameters—including initial pH, catalyst dosage, initial pollutant concentration, reaction time, and temperature.

3.2.1. Effect of operational parameters on the photocatalytic degradation of abamectin

Catalyst Dosage effect

The influence of catalyst dosage on the degradation efficiency of abamectin was investigated under UV/H_2O_2 conditions (Fig. 3a). Degradation efficiency increased significantly as catalyst loading rose to an optimum of 0.03 g, beyond which performance declined.

This behavior reflects competing physical and chemical phenomena. Up to the optimal dosage, a greater density of surface-immobilized iron centers accelerates Fe(II)/Fe(III) redox cycling and enhances the catalytic decomposition of H_2O_2 into reactive hydroxyl radicals (·OH) [30]. Above 0.03 g, excess suspended particles increase reaction-medium turbidity. Simultaneously, at high particle loadings, interparticle agglomeration reduces the accessible active surface area, inducing light-scattering and screening effects that obstruct UV photon penetration and reduce photon utilization efficiency. High particle densities also promote interparticle agglomeration, diminishing the accessible active surface area and imposing mass-transfer limitations on abamectin molecules. Furthermore, an excess of surface iron species can consume ·OH via competing side reactions:

$$Fe^{2+} + {}^{\cdot}OH \rightarrow Fe^{3+} + OH^{-} \quad \text{(Eq. 3)}$$

thereby reducing the net radical concentration available for pollutant degradation [31].

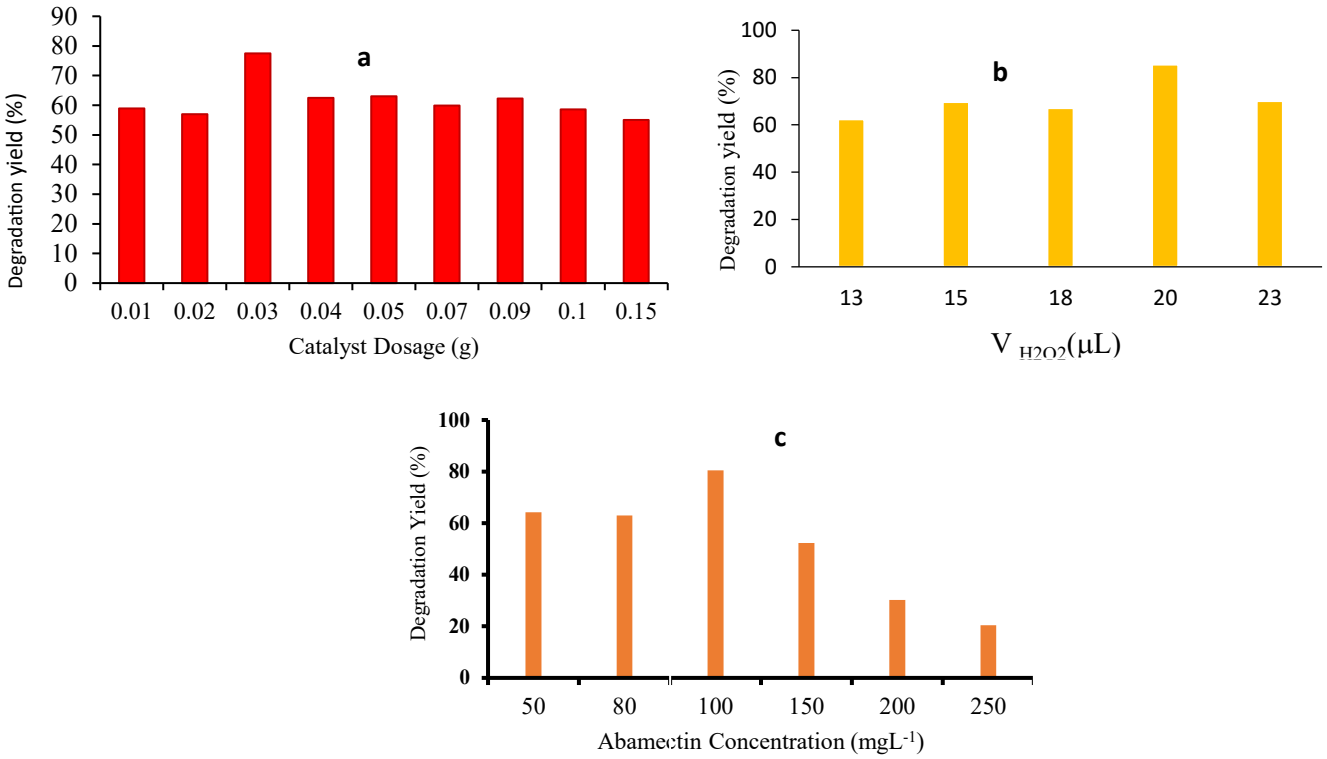

Fig. 3. Optimization of operational parameters on the photocatalytic degradation efficiency of abamectin: (a) effect of catalyst dosage, (b) effect of H_2O_2 dosage, and (c) effect of initial abamectin concentration.

Effect of H_2O_2 Dosage

The effect of hydrogen peroxide concentration on abamectin photocatalytic degradation was investigated by varying the H_2O_2 volume from 13 to 23 µL under fixed conditions (0.03 g Na/Fe-bentonite catalyst, 100 mg L^{-1} abamectin solution, UV irradiation, 180 min). As shown in Fig. 3b, degradation efficiency increased from ~63% at 13 µL to a maximum of ~85% at 20 µL, then declined to ~70% at 23 µL.

The enhancement observed at sub-optimal doses is primarily attributed to two complementary radical-generating pathways. First, direct photolysis of H_2O_2 under UV irradiation produces hydroxyl radicals according to:

$$H_2O_2 + h\nu \rightarrow 2\ {}^{\bullet}OH \qquad \text{(Eq. 4)}$$

Second, the heterogeneous photo-Fenton mechanism proceeds via surface-bound Fe^{2+} sites on the modified bentonite:

$$Fe^{2+} + H_2O_2 \rightarrow Fe^{3+} + {}^{\bullet}OH + OH^- \qquad \text{(Eq. 5)}$$

These two pathways act synergistically, with H_2O_2 functioning as both a direct $^{\bullet}OH$ precursor and an electron acceptor that sustains the Fe^{3+}/Fe^{2+} redox cycle [31, 32]. At the optimum dose of 20 µL, the molar ratio of oxidant to pollutant was calculated to be approximately 17:1 (corresponding to an initial H_2O_2 concentration of ~1.96 mM), which provides sufficient oxidative capacity for effective abamectin degradation.

At doses exceeding 20 µL, however, a significant decline in degradation efficiency was observed. This inhibitory behavior is attributable to two competing scavenging mechanisms. The primary pathway involves the consumption of $^{\bullet}OH$ by excess H_2O_2, generating the considerably less reactive hydroperoxyl radical ($HO_2^{\bullet}$, $E° = 1.65V$ vs. $^{\bullet}OH$, $E° = 2.80V$) [32, 14]:

$$H_2O_2 + \cdot OH \rightarrow HO_2^{\cdot} + H_2O \qquad \text{(Eq. 6)}$$

Additionally, competitive adsorption of excess H_2O_2 molecules onto the iron active sites of the catalyst surface may restrict access of abamectin molecules to these centers, thereby reducing the rate of surface-mediated oxidation reactions [31, 14]. Consequently, 20 µL was selected as the optimum H_2O_2 dose for subsequent experiments.

Effect of abamectin concentration

The influence of initial abamectin concentration (50–250 ppm) on degradation efficiency was investigated under otherwise fixed conditions (0.03 g catalyst, 20 μL H_2O_2, 180min). The efficiency increased from ~ 64% at 50 mg L^{-1} to a maximum of ~ 80% at 100 mg L^{-1}, followed by a decline at higher concentrations (Fig. 3c). The initial enhancement reflects an increased pollutant–radical collision frequency under collision-controlled conditions, whereas beyond the optimum, active-site saturation limits further gain despite the higher substrate load; the efficiency decreased, consistent with the Langmuir–Hinshelwood (L–H) model [33, 34]. This decline is

attributable to (i) saturation of surface-active sites on the Na/Fe-modified bentonite by adsorbed abamectin molecules [35], (ii) a reduced radical-to-pollutant stoichiometric ratio at fixed catalyst and UV output, and (iii) competitive adsorption of partially oxidized intermediates for the limited pool of •OH radicals [4]. Thus, 100 ppm was selected as the optimum concentration in subsequent experiments.

Effect of Initial pH and Its Correlation with Point of Zero Charge (pH_{pzc})

The influence of initial pH on abamectin degradation was examined within the range of 4–9. As illustrated in Fig. 4a, degradation efficiency increased progressively from acidic conditions (~75% at pH 4) toward neutral, reaching a maximum of 85% at pH 7. In alkaline media (pH 8–9), efficiency declined to 76–77%, identifying pH 7 as the optimal condition.

To interpret this behavior, the point of zero charge (pH_{pzc}) of the catalyst was determined by the pH drift method. The ΔpH vs. pH_i curve (Fig. 4b) crosses zero at approximately pH 7, giving:

$$pH_{pzc} \approx 7$$

Below this value, the catalyst surface carries a net positive charge; above it the surface deprotonates and becomes increasingly negative [38, 39].

The coincidence of optimal degradation with pH_{pzc} is not accidental. At this point, the net surface charge of the modified bentonite approaches zero, reducing electrostatic repulsion between the catalyst surface and abamectin molecules. This facilitates access to non-electrostatic active sites — hydrogen bonding and hydrophobic interactions — and creates more favorable conditions for adsorption and hydroxyl radical attack. In acidic media, protonation of the surface suppresses H_2O_2 reactivity and creates electrostatic barriers, while in alkaline conditions two additional mechanisms come into play: deactivation of iron active sites through formation of insoluble iron

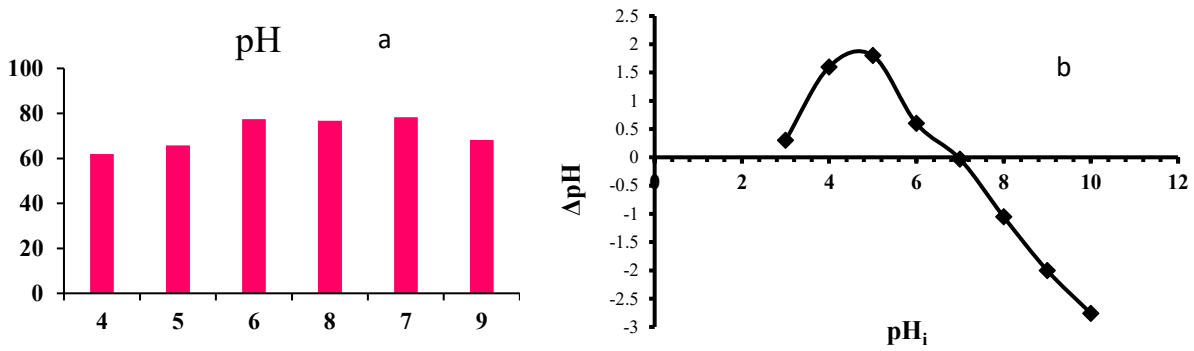

Fig. 4. (a) Effect of initial solution pH on the degradation efficiency of abamectin over Na/Fe-modified bentonite; (b) determination of the point of zero charge $(pH_{pzc})$of Na/Fe-modified bentonite by the initial pH-drift method.

hydroxides, and unproductive decomposition of H_2O_2 into water and molecular oxygen. The efficiency loss at pH values far from neutral therefore cannot be attributed to any single factor [38, 13].

Effect of irradiation time

The influence of irradiation time on abamectin degradation was monitored over a 180-min period under optimized conditions. Before light exposure, the suspension was stirred in the dark to establish adsorption–desorption equilibrium. After light irradiation, degradation was particularly rapid during the initial 90 min, attributable to the high initial pollutant concentration maintaining a steep concentration gradient at the catalyst surface and the abundant generation of hydroxyl radicals under fresh irradiation conditions. Thereafter, the degradation curve gradually leveled off as the residual abamectin depleted and reaction intermediates competed for the remaining catalytic active sites (Fig. 5a). The process approached an apparent plateau around 180 min, which was identified as the optimum irradiation time for maximum pollutant removal.

Effect of Catalyst Type on Photocatalytic Degradation of Abamectin

To separate the contributions of adsorption, oxidation, and photocatalysis to overall removal, we conducted a series of control experiments under identical conditions while systematically omitting one or more system components. In the dark adsorption test (Dark/Catalyst), only ~9% removal was achieved after 150 min, reflecting the limited but non-negligible affinity of abamectin for the clay surface. Adding H_2O_2 in the absence of irradiation (Catalyst/H_2O_2/Dark) raised removal

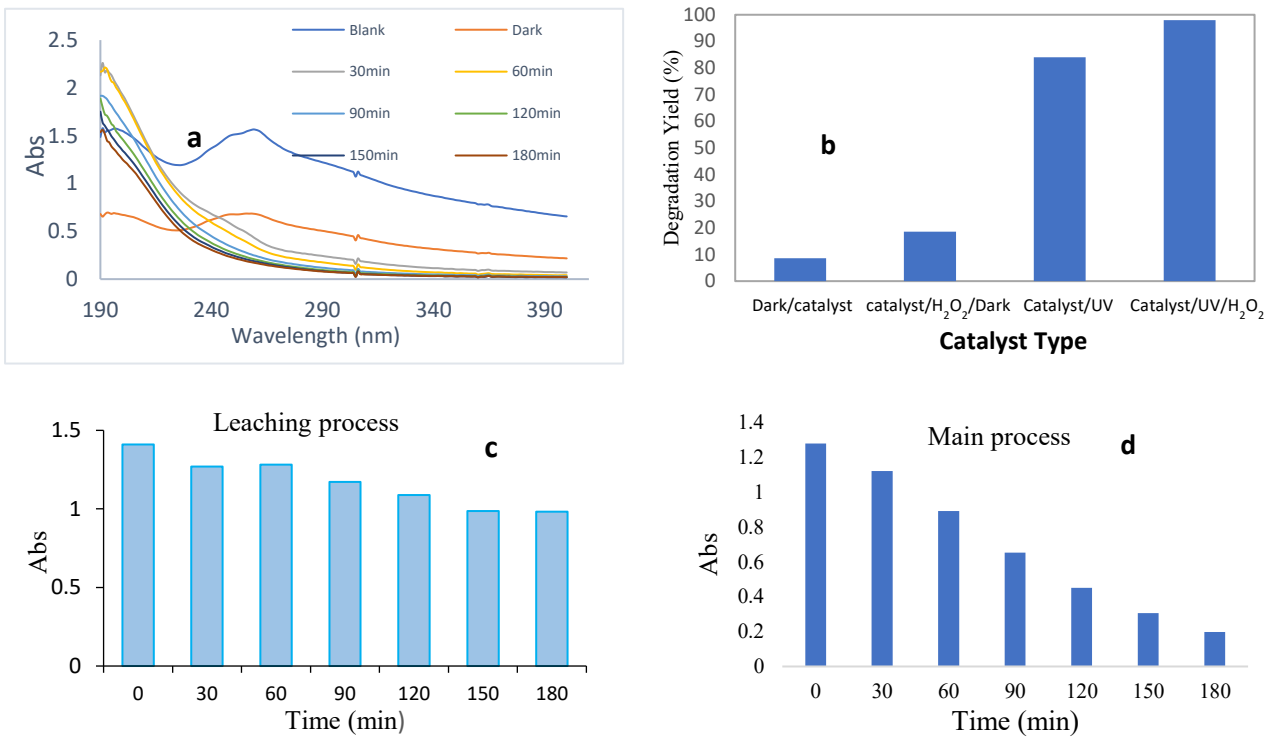

Fig. 5. (a) Time-dependent UV–Vis spectral evolution during abamectin degradation under UV/Na/Fe-bentonite system, (b) comparison of degradation efficiency under different reaction conditions, and (c, d) stability/leaching test comparing abamectin degradation in the main reaction system versus the supernatant after catalyst removal.

marginally to ~17%, confirming that the oxidant alone cannot efficiently degrade the macrocyclic pesticide without photonic activation. Under UV irradiation without H_2O_2 (Catalyst/UV), removal climbed markedly after 180 min, establishing the intrinsic photocatalytic activity of the Na/Fe-modified bentonite: photogenerated electron–hole pairs on the surface iron sites initiate redox reactions that attack the pesticide backbone. The highest performance was reached in the combined Catalyst/UV/H_2O_2 system, where ~98% removal was observed after 180 min (Fig. 5b). This synergy reflects the photo-Fenton-like mechanism operating at the surface iron sites: UV-driven decomposition of H_2O_2 generates •OH radicals in large quantities, which non-selectively cleave the macrocyclic lactone rings of abamectin to reactive organic radicals (R•) and ultimately to mineralized products [13].

The observed order, Dark < H_2O_2/Dark < UV < UV/H_2O_2, clearly demonstrates the complementary roles of UV irradiation and the oxidant in driving the heterogeneous photo-Fenton-like process.

3.2.2. COD and BOD5 measurements

The significant reduction in COD (from 34.6 to 9.02 mg L^{-1}), BOD_5 (from 4.32 to 1.22 mg L^{-1}), and UV–Vis absorbance indicates the efficient oxidative transformation of abamectin, representing a 73.9% decrease in measured COD within the heterogeneous Na/Fe-bentonite/UV/H_2O_2 system. These findings are consistent with previous reports on abamectin degradation in aqueous systems [32,40]. Under UV irradiation, the immobilized iron species on the bentonite surface likely facilitate H_2O_2 activation and the formation of reactive oxidizing species at the catalyst interface, promoting pesticide degradation. While COD and BOD_5 were measured only in the aqueous system, the observed UV–Vis spectral evolution in soil samples is consistent with analogous oxidative processes and suggests the potential applicability of this Na/Fe-modified bentonite system for remediating pesticide-contaminated soils.

3.2.3. Leaching test, structural stability, and catalyst reusability

To elucidate the degradation pathway and assess the catalyst's structural robustness, we performed a catalyst removal (leaching) test at an early stage of the degradation process (t = 30 min). Following filtration of the catalyst, the degradation rate reduced notably, achieving only an additional ~10% abamectin removal over the subsequent 150 min (Fig. 5c). This marked cessation confirms that a heterogeneous surface reaction predominantly drives the degradation at the solid–liquid interface, rather than a homogeneous Fenton-like pathway mediated by dissolved iron ions [18]. This is further substantiated by ICP-OES analysis of the filtrate, which demonstrated

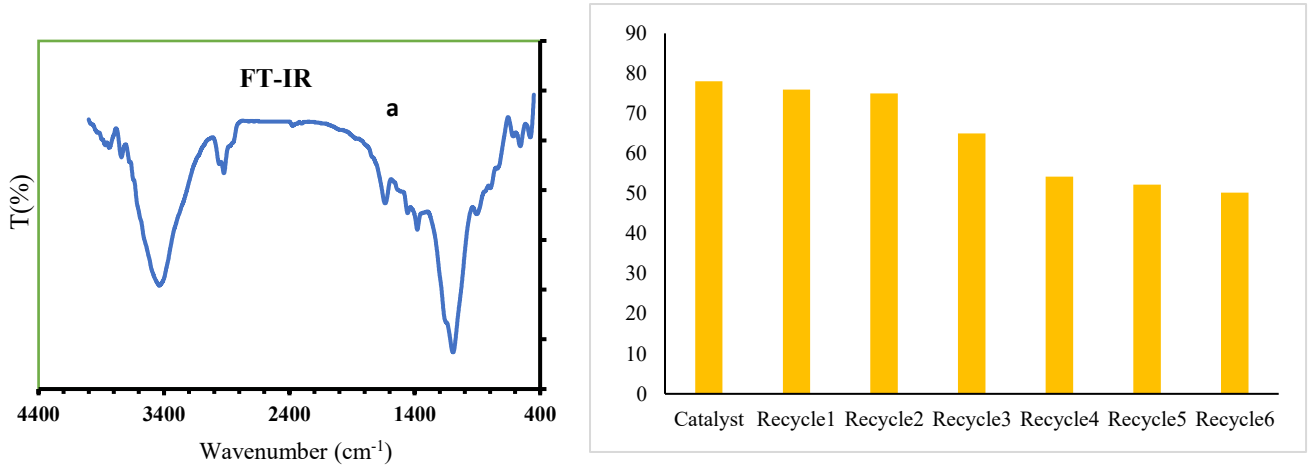

Fig. 6. (a) FT-IR spectrum of the recovered catalyst confirming structural integrity after degradation and (b) Reusability and recycling performance of Na/Fe-modified bentonite over six consecutive catalytic runs

negligible iron leaching (<0.5 mg/L), confirming strong anchoring of the iron species within the bentonite matrix and ruling out homogeneous Fenton contribution.

To investigate post-reaction surface interactions, we analyzed the FT-IR spectrum of the spent catalyst (Fig. 6a) and compared it with the fresh catalyst spectrum presented earlier in the characterization section. Crucially, the characteristic framework vibrational bands of the aluminosilicate matrix—namely the asymmetric stretching vibration at ~1093 cm^{-1} and octahedral bending at ~907 cm^{-1}—remained structurally preserved without observable shift, confirming the stability of the layered clay skeleton under oxidative conditions [41]. Simultaneously, a new absorption band emerged at 2922 cm^{-1}, assigned to aliphatic C–H stretching vibrations. This provides direct spectroscopic evidence for the interfacial adsorption of abamectin molecules and/or their hydrophobic degradation intermediates onto the catalyst surface [42].

This interfacial accumulation of organic moieties provides a clear rationale for the performance trend observed in the reusability cycles (Fig. 6b). The gradual decline in degradation efficiency over consecutive cycles is primarily attributed to surface fouling and active-site masking, where persistent deposition of organic intermediates obstructs substrate accessibility to the active iron centers [43]. Therefore, supported by the leaching results and structural preservation observed in FT-IR, the activity loss across cycles suggests that mild regenerative treatments — such as calcination or solvent washing — could restore the catalytic activity.

3.3. Kinetic Modeling of Abamectin Degradation

The photocatalytic degradation kinetics of abamectin over the synthesized Na/Fe-modified bentonite catalyst were evaluated using the Langmuir–Hinshelwood (L–H) kinetic model. The initial degradation rate (R) as a function of the initial abamectin concentration (C) is expressed as follows [34]:

$$R = -\frac{dc}{dt} = \frac{k_r K_{ads} C}{1 + K_{ads} C} \qquad \text{(Eq. 7)}$$

where C is the concentration of abamectin at time t, K_{ads} represents the Langmuir adsorption equilibrium constant ($L.mg^{-1}$), and k_r denotes the intrinsic surface reaction rate constant ($mg \cdot L^{-1} \cdot min^{-1}$).

At low pollutant concentrations, the term $K_{ads}C \ll 1$ in the denominator of Eq. (7), reducing the expression to an apparent pseudo-first-order kinetic rule:

$$R = -\frac{dC}{dt} = k_{app}C \rightarrow \ln\left(\frac{C_0}{C_t}\right) = k_{app}t \qquad \text{(Eq. 8)}$$

where $k_{app}=k_rK_{ads}$ represents the apparent pseudo-first-order rate constant (min^{-1}). Plotting $\ln(C_0/C_t)$ versus irradiation time (Fig. 7) gave a linear relationship with k_{app} = 0.0089 min^{-1} (R^2 = 0.964) under standard baseline conditions (0.03 g catalyst, 100 $mg \cdot L^{-1}$ abamectin, 20 µL H_2O_2, 25 °C). Concentrations were obtained from the UV–Vis calibration line A = 0.0209C − 0.0129.$\ln(\frac{C_0}{C_t})$

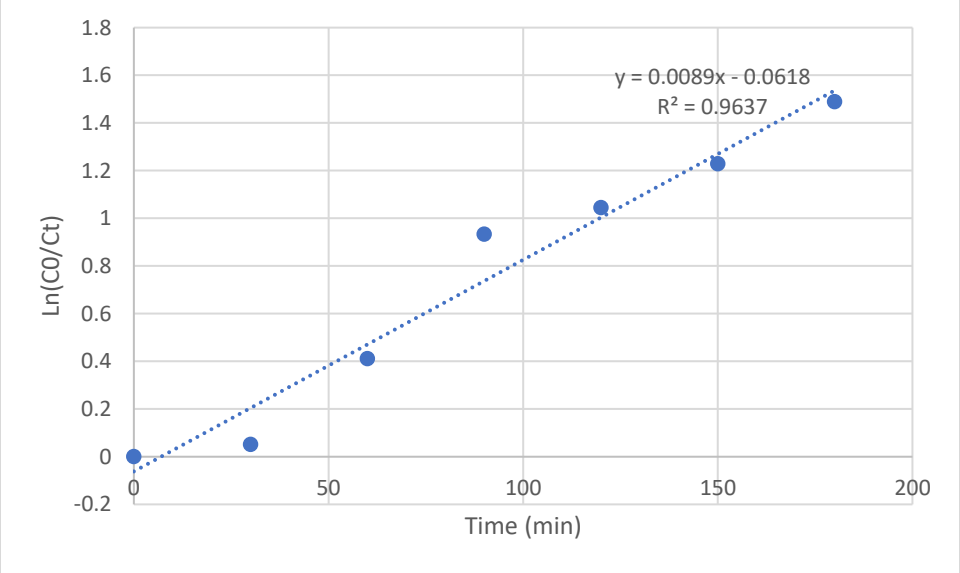

Fig. 7. Apparent pseudo-first-order kinetic plot of ln (C_0/C_t) versus reaction time for the photocatalytic degradation of abamectin over Na/Fe-bentonite.

3. 4. Degradation of Abamectin in Contaminated Soil Using Na/Fe-Modified Bentonite: Evidence for Irreversible Chemical Destruction over Physical Adsorption

Field experiments conducted on contaminated soil (Fig. 9) demonstrated that iron-modified bentonite produced a significant reduction in residual abamectin concentration compared with untreated soil, an effect detectable within the first hour post-application and sustained over a 10-day observation period. Nevertheless, both the rate and extent of removal in the soil matrix were considerably lower than those observed in the controlled aqueous photocatalytic system, where about 78% removal was reached within 180 minutes. This difference is attributed to the inherent complexity of the soil matrix: competition of natural organic matter for photogenerated hydroxyl radicals, restricted UV light penetration through soil particles, and strong pesticide–mineral interactions collectively reduce the efficiency of the Fenton-like photocatalytic pathway relative to a homogeneous aqueous phase [28].

Of particular mechanistic significance is the absence of any rebound in abamectin concentration over the 10-day monitoring period. Had physical adsorption (physisorption) been the dominant removal pathway, the reversible nature of such surface binding would be expected to drive

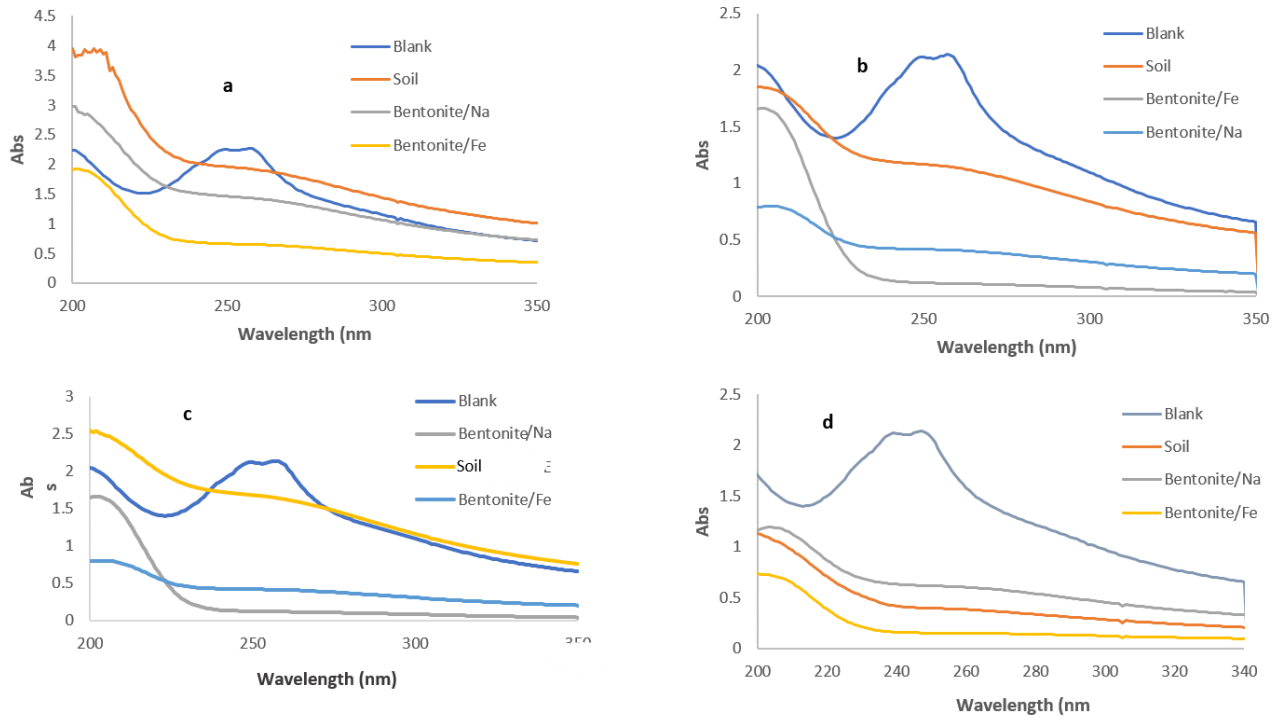

Fig. 9. UV–Vis absorption spectra of abamectin extracted from contaminated soil samples at various degradation time points: (a) 1 h, (b) 24 h, (c) 72 h, and (d) 240 h (10 day) under the UV/Na/Fe-bentonite/H_2O_2 system

progressive desorption back into the pore-water phase as local equilibria were re-established in the soil matrix, yielding a measurable rebound in extractable pesticide concentration. The consistent absence of this rebound effect in Bentonite/Fe-treated samples provides indirect but substantive evidence that irreversible chemical destruction of the abamectin molecule — via Fenton-like radical oxidation — rather than physical entrapment within the clay interlayer, is the predominant removal mechanism. This finding demonstrates that reactive radical-induced oxidation, rather than mere physical adsorption or entrapment within the clay interlayers, serves as the predominant removal mechanism in real soil matrices. It underscores the vital role of the stabilized iron phase in activating hydrogen peroxide and maintaining long-term remediation performance under complex soil environmental conditions [18, 39].

4. Conclusions

In this study, a low-cost natural bentonite was tailored into an efficient heterogeneous photo-Fenton-like catalyst through a facile, two-step cation-exchange route incorporating species. Comprehensive characterization (XRD, FT-IR, BET, and FE-SEM/EDS) supported the structural preservation of the two-dimensional montmorillonite framework, presenting a predominantly mesoporous architecture (SBET= 34.92 m^2 g^{-1}) with uniformly dispersed iron active centers. Moreover, the engineered process demonstrated optimal degradation efficiency under unadjusted, near-neutral conditions (pH = 7), aligning with the catalyst point of zero charge ($pH_{PZC} \approx 7$). This feature successfully overcomes the traditional drawbacks of homogeneous Fenton systems, specifically the acidic pH requirement and iron sludge formation. Under optimized conditions, substantial removal of abamectin was achieved (about 78% at 25 °C), following pseudo-first-order kinetics ($k = 0.0089\ min^{-1}$). Because temperature-dependent data were not collected under matched conditions, ambient temperature was selected. Furthermore, a 73.9% COD reduction and an increased biodegradability ratio (from 0.125 to 0.135) indicated partial mineralization and improved biodegradability of the treated solution.

The genuine heterogeneity of the catalytic system was rigorously verified by filtration leaching tests, which exhibited immediate cessation of degradation following solid separation at 30 min, alongside negligible iron leaching (< 0.5 mg L^{-1}). Post-reaction FT-IR spectroscopy confirmed framework preservation (retention of 1093 and 907 cm^{-1}bands), whereas the appearance of an aliphatic C–H stretching vibration at 2922 cm^{-1}assigned to progressive cyclic activity decay to

surface foulant accumulation (fouling/masking) rather than iron dissolution. Finally, pot soil remediation trials with exposure durations from 1 h to 10 days revealed that while Na-bentonite reached an adsorption saturation plateau after 72 h, the Na/Fe-bentonite system induced continuous dissipation without any concentration rebound effect, suggesting continuous oxidative transformation via heterogeneous Fenton-like pathways as the predominant removal mechanism, in contrast to reversible adsorption observed with Na-bentonite. Collectively, these findings highlight Na/Fe-modified bentonite as a robust, cost-effective, and environmentally promising platform for the sustainable decontamination of pesticide-polluted aquatic and terrestrial environments.

Acknowledgements: The authors sincerely appreciate the support from the Central Research Laboratory at the University of Maragheh for their assistance with the instrumental analyses.

Funding: This research did not receive any specific grant from funding agencies in the public, commercial, or not-for-profit sectors.

Declaration of Competing Interest: The authors declare that they have no known competing financial interests or personal relationships that could have appeared to influence the work reported in this paper.

Declaration of Generative AI and AI-Assisted Technologies in the Writing Process:

During the preparation of this work, the authors used AI-assisted language tools solely to improve the readability, language clarity, and grammatical precision of the manuscript. After using this tool/service, the authors reviewed and edited the content as needed and take full responsibility for the content of the publication.

Data availability

The datasets used and/or analysed during the current study are available from the corresponding author on reasonable request.

References

[1] F.P. Carvalho, Pesticides, environment, and food safety, Food Energy Secur. 6 (2) (2017) 48–60.

[2] M. Grung, Y. Lin, H. Zhang, A.O. Steen, J. Huang, G. Zhang, T. Larssen, Pesticide levels and environmental risk in aquatic environments in China—A review, Environ. Int. 81 (2015) 87–97.

[3] B. Kumari, V.K. Madan, T.S. Kathpal, Status of insecticide contamination of soil and water in Haryana, India, Environ. Monit. Assess. 136 (1–3) (2008) 239–244.

[4] O. Tiryaki, C. Temur, The fate of pesticide in the environment, J. Biol. Environ. Sci. 4 (10) (2010) 29–38.

[5] T. Tišler, I. Eržen, Abamectin in the aquatic environment, Ecotoxicology 15 (6) (2006) 495–502.

[6] R.D. Ji, X.Y. Wang, J.Y. He, T.Z. Zhu, Y.S. Yu, X. Yang, Y.L. Zhang, Experimental study into ultraviolet degradation of abamectin based on absorption spectrum, in: Proc. 11th Int. Symp. Photonics and Optoelectronics (SOPO 2018), CRC Press, Kunming, China, 2018, p. 121.

[7] M. Moosavifar, S. Bagheri, Photocatalytic performance of $H_6P_2W_{18}O_{62}/TiO_2$ nanocomposite encapsulated into beta zeolite under UV irradiation in the degradation of methyl orange, Photochem. Photobiol. 95 (2) (2019) 532–542.

[8] M. Moosavifar, M. Azarmehr, L. Fathyunes, Synergistic effect of isomorphism substitution of double metal Ce and Ti in Y zeolite by post-synthesis treatment for efficient removal of dye contamination, J. Iran. Chem. Soc. 22 (2025) 177–190.

[9] M.A. Oturan, J.J. Aaron, Advanced oxidation processes in water/wastewater treatment, Crit. Rev. Environ. Sci. Technol. 44 (23) (2014) 2577–2641.

[10] D.B. Miklos, C. Remy, M. Jekel, K.G. Linden, J.E. Drewes, U. Hübner, Evaluation of advanced oxidation processes for water reuse applications: Comparison of ozone, UV/H_2O_2, UV/persulfate and ozone/hydrogen peroxide, Water Res. 139 (2018) 118–131.

[11] C. Amor, E. De Torres-Socías, J.A. Peres, M.I. Maldonado, I. Oller, S. Malato, M.S. Lucas, Mature landfill leachate treatment by coagulation/flocculation combined with Fenton and solar photo-Fenton processes, J. Hazard. Mater. 286 (2015) 261–268.

[12] M. Moosavifar, S.M. Heidari, L. Fathyunes, M. Ranjbar, Y. Wang, H. Arandiyan, Photocatalytic degradation of dye pollutant over FeTPP/NaY zeolite nanocomposite, J. Sol-Gel Sci. Technol. 95 (1) (2020) 171–180.

[13] E. Neyens, J. Baeyens, A review of classic Fenton's peroxidation as an advanced oxidation technique, J. Hazard. Mater. 98 (1–3) (2003) 33–50.

[14] A. Babuponnusami, K. Muthukumar, A review on Fenton and improvements to the Fenton process for wastewater treatment, J. Environ. Chem. Eng. 2 (1) (2014) 557–572.

[15] A. Cesaro, V. Naddeo, V. Belgiorno, Wastewater treatment by combination of advanced oxidation processes and conventional biological systems, J. Bioremediat. Biodegrad. 4 (8) (2013) 1–8.

[16] J. Herney-Ramirez, C.A. Costa, L.M. Madeira, G. Mata, M.A. Vicente, M.L. Rojas-Cervantes, A.J. López-Peinado, R.M. Martín-Aranda, Fenton-like oxidation of Orange II solutions using heterogeneous catalysts based on saponite clay, Appl. Catal. B: Environ. 71 (2007) 1-2.

[17] O. Karnland, Chemical and mineralogical characterization of the bentonite buffer for the acceptance control procedure in a KBS-3 repository, SKB Technical Report SKB-TR-10-60, Swedish Nuclear Fuel and Waste Management Co., Stockholm, Sweden, 2010.

[18] Y. Gao, N. Gao, W. Deng, Y. Yang, D. Zhou, Removal of Rhodamine B with Fe-supported bentonite as heterogeneous photo-Fenton catalyst: Mechanisms and performance, *Appl. Catal. B: Environ.* 178 (2015) 29-36.

[19] M. Toor, B. Jin, S. Dai, V. Vimonses, Activating natural bentonite as a cost-effective adsorbent for removal of recalcitrant organic dye in water, J. Ind. Eng. Chem. 21 (2015) 653–661.

[20] J.M. Peralta-Hernández, E. Brillas, Fenton and photo-Fenton strategies for sustainable pesticide decontamination: A review, Chemosphere 394 (2026) 144784.

[21] R.D. Villa, A.G. Trovó, R.F.P. Nogueira, Soil remediation using a coupled process: Soil washing with surfactant followed by photo-Fenton oxidation, J. Hazard. Mater. 174 (1–3) (2010) 770–775.

[22] M. Moosavifar, S. Akbari, M. Nejat-Dehkordi, Optimizing photocatalytic efficiency and durability of zeolite-based catalysts via cation doping for effective dye contaminant removal, J. Inorg. Organomet. Polym. Mater. 35 (2025) 538–551.

[23] APHA, Standard Methods for the Examination of Water and Wastewater: Method 5210 B (5-Day BOD Test) and Method 4500-O C (Azide Modification of the Winkler Method), American Public Health Association, Washington, DC, 2017.

[24] F. Bergaya, G. Lagaly (Eds.), Handbook of Clay Science, second ed., Developments in Clay Science, Vols. 5A–5B, Elsevier, Amsterdam, 2013.

[25] P. Yuan, H. He, F. Bergaya, D. Wu, Q. Zhou, J. Zhu, Synthesis and characterization of delaminated iron-pillared clay with meso–microporous structure, Microporous Mesoporous Mater. 88 (1–3) (2006) 8–15.

[26] D.M. Moore, R.C. Reynolds Jr., X-Ray Diffraction and the Identification and Analysis of Clay Minerals, second ed., Oxford University Press, New York, 1997.

[27] M.J. Wilson (Ed.), A Handbook of Determinative Methods in Clay Mineralogy, Blackie & Son, Glasgow, 1987.

[28] J. Herney-Ramírez, M.A. Vicente, L.M. Madeira, Heterogeneous photo-Fenton oxidation with pillared clay-based catalysts for wastewater treatment: A review, Appl. Catal. B: Environ. 98 (1–2) (2010) 10–26.

[29] M. Thommes, K. Kaneko, A.V. Neimark, J.P. Olivier, F. Rodriguez-Reinoso, J. Rouquerol, K.S.W. Sing, Physisorption of gases, with special reference to the evaluation of surface area and pore size distribution (IUPAC Technical Report), Pure Appl. Chem. 87 (9–10) (2015) 1051–1069.

[30] Y. Zhang, H. Xiang, F. Ke, C. Song, J. Liu, X. Zhou, Fe-pillared bentonite as an efficient heterogeneous photo-Fenton catalyst for degradation of organic pollutants: Interlayer structure and catalytic mechanisms, Appl. Clay Sci. 198 (2020) 105820.

[31] J.J. Pignatello, E. Oliveros, A. MacKay, Advanced oxidation processes for organic contaminant destruction based on the Fenton reaction and related chemistry, Crit. Rev. Environ. Sci. Technol. 36 (1) (2006) 1–84.

[32] T.A.F. Matos, A.L.N. Dias, A.D.P. Reis, M.R.A. Silva, M.M. Kondo, Degradation of abamectin using the photo-Fenton process, Int. J. Chem. Eng. 2012 (2012) 915724.

[33] M.R. Hoffmann, S.T. Martin, W. Choi, D.W. Bahnemann, Environmental applications of semiconductor photocatalysis, Chem. Rev. 95 (1) (1995) 69–96.

[34] J.M. Herrmann, Heterogeneous photocatalysis: Fundamentals and applications to the removal of various types of aqueous pollutants, Catal. Today 53 (1) (1999) 115–129.

[35] N. Daneshvar, D. Salari, A.R. Khataee, Photocatalytic degradation of azo dye acid red 14 in water on ZnO as an alternative catalyst to TiO_2, J. Photochem. Photobiol. A: Chem. 162 (2–3) (2004) 317–322.

[36] G. Lagaly, Pesticide–clay interactions and formulations, Appl. Clay Sci. 18 (5–6) (2001) 205–209.

[37] S. Malato, P. Fernández-Ibáñez, M.I. Maldonado, J. Blanco, W. Gernjak, Decontamination and disinfection of water by solar photocatalysis: Recent overview and trends, Catal. Today 147 (1) (2009) 1–59.

[38] M. Kosmulski, Surface Charging and Points of Zero Charge, CRC Press, Boca Raton, 2018.

[39] G.A. Parks, The isoelectric points of solid oxides, solid hydroxides, and aqueous hydroxo complex systems, Chem. Rev. 65 (2) (1965) 177–198.

693 [40] A. Boukhemkhem, E.L. Bedia, Degradation of pesticides by heterogeneous Fenton using iron-
694 exchanged bentonites, Appl. Clay Sci. 114 (2015) 308–316.

695 [41] J. Madejová, FTIR techniques in clay mineral studies, Vib. Spectrosc. 31 (1) (2003) 1–10.

696 [42] R.M. Silverstein, F.X. Webster, D.J. Kiemle, D.L. Bryce, Spectrometric Identification of
697 Organic Compounds, eighth ed., John Wiley & Sons, Hoboken, NJ, 2014.

698 [43] M.D. Argyle, C.H. Bartholomew, Heterogeneous catalyst deactivation and regeneration: A
699 review, Catalysts 5 (1) (2015) 145–269.

Supplementary Files

This is a list of supplementary files associated with this preprint. Click to download.

- suplamentary.docx